Correlation function approach for diffusion in confined geometries

Bruce J. Palmer,[1] Jaehun Chun,[1,2] Jeffrey F. Morris,[2] Christopher J. Mundy,[1] and Gregory K. Schenter[1]
[1]*Pacific Northwest National Laboratory, Richland, Washington 99354, USA*
[2]*Levich Institute and Department of Chemical Engineering, CUNY City College of New York, New York 10031, USA*

(Received 15 May 2020; accepted 23 July 2020; published 19 August 2020)

This paper describes a formalism for extracting spatially varying transport coefficients from simulations of a molecular fluid in a nanochannel. This approach is applied to self-diffusion of a Lennard-Jones fluid confined between two parallel surfaces. A numerical grid is laid over the domain confining the fluid, and fluid properties are projected onto the grid cells. The time correlation functions between properties in different grid cells are calculated and can be used as the basis for a fitting procedure for extracting spatially varying diffusion coefficients from the simulation. Results for the Lennard-Jones system show that transport behavior varies sharply near the liquid-solid boundary and that the changes depend on the details of the liquid-solid interaction. A quantitative difference between the reduced and detailed models is discussed. It is found that the difference could be associated with assumptions about the form of the transport equations at molecular scales in lieu of problems with the method itself. The study suggests that this approach to fitting molecular simulations to continuum equations may guide the development of appropriate coarse-grained equations to model transport phenomena at nanometer scales.

DOI: 10.1103/PhysRevE.102.022129

I. INTRODUCTION

The properties of fluids in confined geometries, such as nanochannels, pores, or a lubricated region between two interfaces, are of considerable scientific and technical interest. Transport phenomena in geometries with dimensions that are within an order of magnitude of the size of individual molecules [i.e., $\sim O(1)$ nm] are important in understanding many biological [1], manufacturing [2], energy storage [3], and environmental systems [4]. However, formidable theoretical challenges remain in understanding transport behavior in confined geometries. The conventional framework of molecular simulation is limited by the challenge of establishing experimentally relevant solution conditions and the representation of local chemical potentials in confined heterogeneous environments [5–9]. A single simulation may require hundreds of thousands of atoms to simulate the behavior of even relatively simple systems. Furthermore, because the systems are large, many slow timescales (i.e., collective phenomena) begin to appear in them and these can require very long simulations in order to obtain good statistics on their behavior.

Alternatively, continuum-based approaches can be more attractive for simulating such confined geometries. These methods rely on integrating out the fast timescales at the molecular scale. However, under nanoconfinement many of the timescales and length scales become coupled (e.g., the fundamental assumption of infinitesimally small molecular constituents breaks down) and molecular detail becomes significant. Specifically, the notion that fluid properties such as density and viscosity are uniform everywhere in the system and that hydrodynamic fields are varying slowly over dimensions that are large compared to individual molecules are no longer valid assumptions. Nevertheless, continuum approaches have the advantage that it would be possible, in principle, to simulate systems that are clearly beyond the capabilities of direct atomistic simulation, provided continuum theories that are enhanced with molecular descriptors are formulated.

Previous simulations of fluids in confined geometries have indicated that behavior of the fluid will depart from the bulk liquid when geometries approach the scale of a few molecules [10–13]. Liquids are known to become more structured near any surface. Additionally, the chemical properties of the surface, such as the charge state, can further complicate the coupling between the fluid and the surface at the molecular scale and can be expected to alter the mechanical and transport properties of the fluid over short distances. In a nanoconfined geometry, where essentially all fluid molecules are influenced by an interface, these altered properties will dominate the behavior of the system. A large body of simulation work supports this notion [7,14–16]. Fluids near surfaces are markedly different from the bulk and these differences can extend over many molecular diameters [13,17–20]. Furthermore, charge accumulation and other physicochemical properties of the surface can alter the excess chemical potential of species in the vicinity of the surface, resulting in vastly different macroscopic behavior than that experienced under bulk conditions. To this end, completely unexpected dynamic behavior (e.g., viscoelasticity and diffusivity) that is dependent on surface and solution chemistry has been observed for aqueous solutions and hydrocarbons [18,21–25].

To date, most studies of the microscopic basis of transport have focused on the properties of bulk fluids in a regime where it is possible to define a fluid volume element that

is much larger than the dimensions of individual molecules. The original theories developing the correlation function expressions for transport coefficients, such as those of Green [26,27] and later Kubo [28] and Zwanzig [29] relied on the concept of using a plane-wave expansion of fluctuations and taking the limit that the wave number goes to zero (i.e., an infinite system). More recently, Gao and Limmer have used large deviation functions to generate sampling protocols to enhance convergence of transport coefficient calculations for a system far from equilibrium [30,31]. This approach is based on a generating functional that is used to construct biased sequences of trajectories that can be used to extract transport coefficient values. An advantage of this approach is that it can be generalized to include nonlinear responses but at this time the method is still restricted to uniform systems.

A different approach was taken by Español *et al.* [32–34], who looked at projecting fluctuations onto finite element basis functions. However, this work still required finite elements that were large enough to minimize the effects of troublesome surface terms due to interactions at the boundary with other grid cells. This condition is equivalent to a requirement that the grid cells should be much larger than the scale of individual molecules. Although the use of a numerical grid opened up the possibility of incorporating spatial variability, the approximations and assumptions required to achieve an analytically tractable result limited its applicability to uniform systems. Pu *et al.* [24] directly targeted nonuniform systems and developed a theory for determining spatially varying diffusion coefficients in confined geometries by evaluating the mean square displacement of molecules in slabs parallel to the surface. Unfortunately, their method relies heavily on the connection between the mean square displacement and diffusion coefficient (i.e., the Einstein relation), limiting its applicability for other types of transport.

Transport phenomena at small scales have also been studied using fluctuating hydrodynamics, originally proposed by Landau and Lifshitz [35]. This can be used to include random fluctuations, associated with the discrete molecular nature of fluids, in dissipative contributions to fluxes. The fluctuations are chosen so as to be consistent with the fluctuation-dissipation theorem. While intriguing, fluctuating hydrodynamics based approaches [36,37] that were applied to confined geometries such as nanochannels or pores do not reflect (i) the unique and anomalous physicochemical nature of confined fluids and (ii) the relation between constitutive relations and boundary conditions while maintaining a framework similar to the continuum transport equations (i.e., a partial differential equation form).

Previous work by one of us [38] looked at the use of basis functions restricted to the cells of a numerical finite volume grid to calculate localized transport properties. This use of grid cells resembles the finite element approach taken by Español *et al.*, but unlike them we focused specifically on situations where the conditions for the hydrodynamic limit do not apply. As an illustrative calculation, the concentration field of a diffusing species in a model one-dimensional (1D) system was projected onto the cells of an evenly spaced grid overlaying the simulation. Correlation functions of the concentration in different grid cells were calculated from the simulations and the correlation matrix formed by integrating these functions over all time could be related to the spatially varying diffusion operator for the system. This calculation was shown to work for small systems but is probably not practical for realistic atomic or molecular fluids in three dimensions (3D). The extension of this work to realistic models of liquids is the focus here.

This paper will look at fitting the diffusion operator directly to the correlation functions instead of using their integrals. This approach is more complicated but it eliminates some major problems, the main one being the need for sufficiently long simulations to ensure the complete decay of all correlation functions. Fitting the time correlation functions directly allows one to ignore the long time tails, which can reduce the computational burden considerably. The general approach proposed here can also be applied, at least in principle, to more complicated transport and flow models as well as to more complicated fluids. Important examples are electrolyte solutions confined between mineral surfaces or in a porous component of an energy storage device. Flow models might be extended to contain nonlocal expressions for the constitutive relations, electrostatic forces between dissolved species and surface charges, and other couplings between hydrodynamic fields such as concentration, velocity, and temperature.

II. MATHEMATICAL FORMULATION

A. Fluctuation-based fitting formalism

This section will provide a brief review of a general method for connecting correlation functions constructed from grid cells to nanoscale hydrodynamic equations. This formalism is similar to other approaches [39–41], although most of these studies have focused on projecting fluids onto plane waves [42–45]. Correlation functions can be constructed by taking the projections of fluid properties onto the cells of a structured grid, such as the ones used for finite volume or finite element simulations of fluid flow, and then calculating the correlations of different properties for different grid cells at different times. Examples of fluid properties consist of the density, velocity, temperature, and concentration. If the cells are small enough, these properties will fluctuate significantly as a function of time, even for a system in equilibrium, and the correlation functions of these fluctuations can be used to determine properties of the governing equations for the system.

Assume that the fluctuations are small enough that the hydrodynamic evolution operator describing the decay of such fluctuations is linear and that it has no explicit time dependence. The system obeys an equation of the form

$$\frac{\partial X}{\partial t} = LX, \tag{1}$$

where X is a collection of continuum fields and L is a linear operator. The discretized form of Eq. (1) is

$$\frac{\partial \overline{X}}{\partial t} = \overline{\overline{L}} \cdot \overline{X} + \overline{B}, \tag{2}$$

where $\overline{X}$ is a vector of coefficients and $\overline{\overline{L}}$ is a constant matrix corresponding to the linearized operator describing the behavior of the small fluctuations. The vector $\overline{B}$ is a constant

vector that may appear after applying boundary conditions to the discrete set of equations. Performing a Laplace transform on Eq. (2) and solving for $\overline{X}(z)$ gives the algebraic equation

$$\overline{X}(z) = \frac{1}{z - \overline{\overline{L}}} \cdot \overline{X}(t=0) + \frac{1}{z(z - \overline{\overline{L}})} \cdot \overline{B}. \tag{3}$$

The real-time equivalent of Eq. (3) is

$$\overline{X}(t) = e^{t\overline{\overline{L}}} \cdot \overline{X}(t=0) + (e^{t\overline{\overline{L}}} - 1) \cdot \overline{\overline{L}}^{-1} \cdot \overline{B}. \tag{4}$$

The inverse of $\overline{\overline{L}}$ in Eq. (4) can potentially cause problems if the quantity represented by $\overline{X}$ is conserved. In this case, $\overline{\overline{L}}$ will contain a zero eigenvalue. However, in order for $\overline{X}$ to be conserved, the fluxes into and out of the system must vanish and this will mean that $\overline{B}$ is zero. Furthermore, as shown below, even in the case that $\overline{B}$ is nonzero, the term will drop out if $\overline{X}$ represents fluctuations about the mean.

Let $X_i(t)$ be the ith component of $\overline{X}(t)$. If the $X_i(t=0)$ are taken from an ensemble of fluctuations in the system, the time correlation functions of the X_i have the form [38,41]

$$\langle X_i(t)X_j(t=0)\rangle = \sum_k [e^{\overline{\overline{L}}t}]_{ik} \langle X_k(t=0)X_j(t=0)\rangle + \sum_k [(e^{\overline{\overline{L}}t} - 1) \cdot \overline{\overline{L}}^{-1}]_{ik} \langle B_k X_j(t=0)\rangle. \tag{5}$$

Defining the equilibrium set of fluctuations as

$$\Delta_{ij} = \langle X_i(t=0)X_j(t=0)\rangle$$

and the time correlation functions as

$$C_{ij}(t) = \langle X_i(t)X_j(t=0)\rangle$$

then the time correlation functions, equilibrium fluctuations, and the matrix $\overline{\overline{L}}$ are all related via the expression

$$\overline{\overline{C}}(t) = e^{\overline{\overline{L}}t} \cdot \overline{\overline{\Delta}}. \tag{6}$$

Since $\overline{B}$ is a constant, the last term in Eq. (5) drops out if the fluctuations represented by $\overline{X}(t)$ have zero mean.

The Laplace transform of this equation is

$$\overline{\overline{C}}(z) = \frac{1}{z - \overline{\overline{L}}} \cdot \overline{\overline{\Delta}}$$

and the limit of $z \to 0$ gives

$$\overline{\overline{C}}(z=0) = -\overline{\overline{L}}^{-1} \cdot \overline{\overline{\Delta}}. \tag{7}$$

The value of a Laplace transform at $z = 0$ is equivalent to the integral from $t = 0$ to infinity of the corresponding real-time function, so Eq. (7) provides a relation between the linear evolution operator, the fluctuation matrix $\overline{\overline{\Delta}}$, and the integral over all time of the correlation matrix $\overline{\overline{C}}$. Both $\overline{\overline{C}}$ and $\overline{\overline{\Delta}}$ can be measured from simulations and so $\overline{\overline{L}}$ could, in principle, be calculated using Eq. (7). This was explored in our previous work [38]. Because calculating all correlation functions accurately enough to get reliable values for the matrix $\overline{\overline{C}}(z=0)$ was not feasible, a fitting procedure using only correlation functions between nearby grid cells was developed. These correlation functions tended to have large amplitudes and faster timescales so that values for the correlation with good statistics could be obtained using relatively short simulations. For the simple one-dimensional system investigated in the previous work, this was sufficient to recover an accurate representation of the spatially varying diffusion coefficient.

However, this approach had several features that made it problematic for realistic simulations involving molecular fluids. First, the original model problem consisted of a 1D cellular automata that could be easily simulated for extremely long times, allowing accurate enough simulations of the correlation functions to obtain reliable values for their time integrals. Second, the need to obtain reliable values for the integrals also implied that all measured correlation functions had to be simulated for long enough periods that they had effectively decayed to zero. Finally, the fitting procedure required the evaluation of the inverse of the evolution operator $\overline{\overline{L}}$. For conserved quantities, the evolution operator has a zero in its eigenvalue spectrum that requires additional handling. All of those features suggested that inferring $\overline{\overline{L}}$ directly using Eq. (7) would not be successful for a 3D system with molecular fluids.

To overcome these difficulties, we developed an approach to make direct use of Eq. (6). The discrete evolution operator $\overline{\overline{L}}$ is assumed to depend on a collection of parameters, written as a vector $\overline{a}$, that will be determined by a fit of $\overline{\overline{L}}$ to a set of measured correlation functions. The objective function for this fit has the form

$$\chi(\overline{a}) = \sum_s \sum_{\{i,j\}} ([e^{\overline{\overline{L}}(\overline{a})t_s} \cdot \overline{\overline{\Delta}}]_{ij} - \tilde{C}_{ij}(t_s))^2, \tag{8}$$

where the index s runs over a set of time measurements, $\{i, j\}$ is a set of grid cell pairs (indexed by i and j), and the $\tilde{C}_{ij}$ are measured correlation functions. The set $\{i, j\}$ is a subset of all possible cell pairs and is restricted in these studies to cells that are close to each other. In this paper, the adjustable parameters $\overline{a}$ in the evolution operator correspond to the values of the diffusion coefficient matrix in each of the grid cells. For the slit pore geometry, the grid cell indices are actually triples i, j, k representing the indices along the x, y, z axes.

Fitting the real-time correlation functions has one major advantage over the previous method based on integrals of the $C_{ij}(t)$. It is no longer necessary to run the simulations long enough to accurately simulate the tails of the correlation functions in order to obtain reliable values for the integrals. The set of correlation pairs can be cut off at some time value even if not all correlation functions have decayed to zero; this has a significant impact on the amount of time that must be spent in the simulation for good statistics. The tradeoff is that the simulation must still be run for a long enough period of time to ensure that the fitted operator accurately reflects the slower relaxations in the system. These slower timescales reflect the hydrodynamic parts of the transport.

B. Discretized diffusion operator

The system that is modeled in this work consists of a channel that is periodic in the x and y directions and bounded in the z direction by two parallel surfaces. The channel is rectangular and is overlaid with a regular grid with increments

Δx, Δy, Δz. Each grid cell has a volume $V = \Delta x \Delta y \Delta z$ and the faces of the grid cell have areas $A_x = \Delta y \Delta z$, $A_y = \Delta x \Delta z$, $A_z = \Delta x \Delta y$. The most general diffusion equation describing this system will contain a spatially varying diffusion tensor. The system is assumed to have no directional variation in the x and y directions, which implies that the diffusion tensor has the form

$$\overline{\overline{D}} = \begin{bmatrix} \alpha & 0 & 0 \\ 0 & \alpha & 0 \\ 0 & 0 & \beta \end{bmatrix}. \tag{9}$$

The tensor is defined at the center of each grid cell, so each grid cell has two diffusion parameters, α_{ijk} and β_{ijk}, associated with it.

The continuum diffusion equation governing this system is

$$\begin{aligned} \frac{\partial c}{\partial t} &= \nabla \cdot \overline{\overline{D}} \cdot \nabla c \\ &= \left[\frac{\partial}{\partial x} \alpha \frac{\partial}{\partial x} + \frac{\partial}{\partial y} \alpha \frac{\partial}{\partial y} + \frac{\partial}{\partial z} \beta \frac{\partial}{\partial z} \right] c \end{aligned} \tag{10}$$

with the corresponding time evolution operator

$$L = \nabla \cdot \overline{\overline{D}} \cdot \nabla. \tag{11}$$

The diffusion matrix $\overline{\overline{D}}$ depends on position so it does not commute with the spatial derivatives. The operator L is combined with a zero-flux (i.e., Neumann) boundary condition, no mass flux perpendicular to the boundary. This is equivalent to an assumption that particles are neither absorbed nor emitted by the boundary.

The discretized form of L is created using a finite volume approach. Conservation of mass requires that the change in concentration in a grid cell is equal to the sum of the fluxes into and out of the grid cell through the cell faces. This can be written as the expression

$$\begin{aligned} V[c(t + \Delta t) - c(t)] = -(&f_{x+} A_x + f_{x-} A_x + f_{y+} A_y \\ &+ f_{y-} A_y + f_{z+} A_z + f_{z-} A_z) \Delta t, \end{aligned}$$

where f_{x+} is defined as the flux *out* of the cell at time t through the face perpendicular to the x axis and located on the $+$ side of the cell (the direction of increasing x). The remaining fluxes are defined similarly. In the limit that $\Delta t \to 0$, this reduces to the ordinary differential equation

$$V \frac{dc}{dt} = -(f_{x+} A_x + f_{x-} A_x + f_{y+} A_y + f_{y-} A_y + f_{z+} A_z + f_{z-} A_z). \tag{12}$$

The concentration in each cell satisfies an equation of this form. The diffusive flux is the diffusion coefficient times the gradient of the concentration, where the concentration is defined at the center of each grid cell. The gradient can be calculated using a finite difference approach. The gradient along the x axis can be written as

$$\frac{\partial c}{\partial x} \approx \frac{c_{i+1,j,k} - c_{i,j,k}}{\Delta x},$$

where i, j, k are the indices locating the cell in the grid. This approximate formula represents the gradient at the midpoint between the neighboring grid cells at $i + 1$, j, k and i, j, k. To calculate the flux at the surface, we take the average of the diffusion parameters at $i + 1$, j, k and i, j, k. The diffusive flux out of the cell at i, j, k through the $x+$ face is therefore

$$f_{x+}^{i,j,k} = -\frac{c_{i+1,j,k} - c_{i,j,k}}{\Delta x} \frac{\alpha_{i+1,j,k} + \alpha_{i,j,k}}{2}. \tag{13}$$

Combining Eqs. (12) and (13) and expressing the areas of the faces in terms of Δx, Δy, Δz leads to the following equation:

$$\begin{aligned} \frac{dc_{i,j,k}}{dt} = &\frac{\alpha_{i+1,j,k} + \alpha_{i,j,k}}{2} \frac{c_{i+1,j,k} - c_{i,j,k}}{\Delta x^2} \\ &+ \frac{\alpha_{i-1,j,k} + \alpha_{i,j,k}}{2} \frac{c_{i-1,j,k} - c_{i,j,k}}{\Delta x^2} \\ &+ \frac{\alpha_{i,j+1,k} + \alpha_{i,j,k}}{2} \frac{c_{i,j+1,k} - c_{i,j,k}}{\Delta y^2} \\ &+ \frac{\alpha_{i,j-1,k} + \alpha_{i,j,k}}{2} \frac{c_{i,j-1,k} - c_{i,j,k}}{\Delta y^2} \\ &+ \frac{\beta_{i,j,k+1} + \beta_{i,j,k}}{2} \frac{c_{i,j,k+1} - c_{i,j,k}}{\Delta z^2} (1 - \delta_{kN}) \\ &+ \frac{\beta_{i,j,k-1} + \beta_{i,j,k}}{2} \frac{c_{i,j,k-1} - c_{i,j,k}}{\Delta z^2} (1 - \delta_{k1}). \end{aligned} \tag{14}$$

The factors of $(1 - \delta_{k1})$ and $(1 - \delta_{kN_z})$ are included to indicate which terms drop out due to the zero-flux boundary conditions at the interfaces. The lack of any constant terms in this equation confirms the statement in the previous section that the vector $\overline{B}$ vanishes in the case of conserved quantities. The elements of the matrix $\overline{\overline{L}}$ can be read directly from Eq. (14). The dimensions of the grid are assumed to be N_x, N_y, N_z. Because any triple i, j, k can be mapped to a single index n and vice versa, the matrix elements of the discretized version of L can be expressed using the triples as indices. In this formulation, an element of $\overline{\overline{L}}$ can be written as $L_{i,j,k:l,m,n}$, where i, j, k maps to the row index and k, l, m maps to the column index.

C. Problem size reduction

In order to evaluate the objective function, it is necessary to calculate the matrix

$$e^{\overline{\overline{L}} t} \cdot \overline{\overline{\Delta}} \tag{15}$$

for different values of t. This can be done using the diagonalizing transform

$$\overline{\overline{\Lambda}} = \overline{\overline{R}}^{\dagger} \cdot \overline{\overline{L}} \cdot \overline{\overline{R}},$$

where $\overline{\overline{\Lambda}}$ is the diagonal matrix of eigenvalues of $\overline{\overline{L}}$ and $\overline{\overline{R}}$ is the corresponding matrix of eigenvectors. The superscript † indicates a Hermitian transpose matrix. Using this transformation, Eq. (15) becomes

$$e^{\overline{\overline{L}} t} \cdot \overline{\overline{\Delta}} = \overline{\overline{R}} \cdot e^{\overline{\overline{\Lambda}} t} \cdot \overline{\overline{R}}^{\dagger} \cdot \overline{\overline{\Delta}}. \tag{16}$$

Since $\overline{\overline{\Lambda}}$ is diagonal, the exponential in Eq. (16) is easily evaluated. For a grid consisting of $N_x N_y N_z$ cells, the matrix $\overline{\overline{R}}$ will consist of $N_x^2 N_y^2 N_z^2$ elements and it will take approximately $N_x^3 N_y^3 N_z^3$ operations for the diagonalization. For the calculations described below, the values of N_x, N_y, and N_z are 30, 30, and 36, respectively, so the dimension of $\overline{\overline{R}}$ is

32 400. This is a large matrix and it is worth considering how the problem size can be reduced. Fortunately, the slit pore geometry can be exploited to produce a much smaller calculation.

The main strategy for reducing the problem size is to make use of the fact that the system is uniform in the plane parallel to the solid surfaces. However, it is still important to treat the system as having a realistic extent in the xy directions since the behavior of the correlation functions will depend on these dimensions. From a simulation point of view, it is desirable that the system is of reasonable size in the xy plane so that artifacts due to periodic boundary conditions can be minimized.

The assumption of system translational invariance parallel to the surface implies that the diffusion components only depend on the cell index k in the z direction instead of all three indices i, j, k. The concentrations in each grid cell, c_{ijk}, can be written using a plane-wave expansion in the x and y coordinates

$$c_{ijk} = \sum_{l=0}^{N_x-1} \sum_{m=0}^{N_y-1} \gamma_{lmk} e^{I2\pi il/N_x} e^{I2\pi jm/N_y}. \tag{17}$$

The symbol I is used to represent $\sqrt{-1}$ and γ_{lmk} are the expansion coefficients of the c_{ijk}. Combining Eq. (17) and the equation of motion [i.e., Eq. (14)] and equating the coefficients of the exponentials gives the set of coupled equations

$$\begin{aligned}\frac{\partial \gamma_{lmk}}{\partial t} = {} & \frac{\alpha_k}{\Delta x^2}\left[2\cos\left(\frac{2\pi l}{N_x}\right) - 2\right]\gamma_{lmk} + \frac{\alpha_k}{\Delta y^2}\left[2\cos\left(\frac{2\pi m}{N_y}\right) - 2\right]\gamma_{lmk} \\ & + \frac{\beta_{k+1} + \beta_k}{2\Delta z^2}(\gamma_{lm,k+1} - \gamma_{lmk})(1 - \delta_{kN_z}) + \frac{\beta_{k-1} + \beta_k}{2\Delta z^2}(\gamma_{lm,k-1} - \gamma_{lmk})(1 - \delta_{k1}).\end{aligned} \tag{18}$$

There is no coupling between different values of l and m so this set of equations factorizes into a collection of $N_x \times N_y$ blocks of equations. Each block contains N_z equations. The solution procedure is still based on diagonalizing each block, but instead of diagonalizing a matrix of dimension $N_xN_yN_z$ the solution can be found by diagonalizing N_xN_y matrices, each of size N_z. This is both substantially faster [i.e., $O(N_xN_yN_z^3)$ vs $O(N_x^3N_y^3N_z^3)$ operations] as well as requiring much less memory [i.e., $O(N_xN_yN_z^2)$ vs $O(N_x^2N_y^2N_z^2)$ values].

For a given l and m, the coupled equations can be written in matrix form as

$$\frac{\partial \overline{\gamma}_{lm}}{\partial t} = \overline{\overline{\Gamma}}_{lm} \cdot \overline{\gamma}_{lm}, \tag{19}$$

where $\overline{\overline{\Gamma}}_{lm}$ is the matrix of coefficients of the γ_{lmk} in Eq. (18). A separate matrix is generated for each set of indices lm. The corresponding solution is

$$\gamma_{lmk}(t) = \sum_{q=1}^{N_z} [e^{\overline{\overline{\Gamma}}_{lm}t}]_{kq} \gamma_{lmq}(0). \tag{20}$$

The correlation functions for the concentration can then be written as

$$\langle c_{ijk}(t) c_{lmn}(0)\rangle = \sum_{i'=0}^{N_x-1} \sum_{j'=0}^{N_y-1} \sum_{l'=0}^{N_x-1} \sum_{m'=0}^{N_y-1} \sum_{q=1}^{N_z} [e^{\overline{\overline{\Gamma}}_{i'j'}t}]_{kq} \langle \gamma_{i'j'q}\gamma_{l'm'n}\rangle e^{I2\pi i'i/N_x} e^{I2\pi j'j/N_y} e^{I2\pi l'l/N_x} e^{I2\pi m'm/N_y}. \tag{21}$$

Further progress can be made by evaluating the equilibrium correlations $\langle \gamma_{i'j'q}\gamma_{l'm'n}\rangle$ in terms of the equilibrium fluctuation matrix $\overline{\overline{\Delta}}$. Because of the assumption that everything is uniform in the xy plane, the elements of $\overline{\overline{\Delta}}$, $\Delta_{i,j,k:l,m,n}$, only depend on the separations $i - l$ and $j - m$. This implies that they satisfy the relation

$$\Delta_{ijq:lmn} = \Delta_{11q:1+l-i,1+m-j,n}$$

for all values of i, j, l, m. The selection of $i = 1$ and $j = 1$ as the reference cell is arbitrary and any column of cells could have been used. The translation property can be used to simplify the expression for the $\langle \gamma_{i'j'q}\gamma_{l'm'n}\rangle$ in terms of the original matrix elements of $\overline{\overline{\Delta}}$. The γ_{lmq} can be written in terms of the c_{ijk} using the inverse of the discrete Fourier transform. This leads to the expression

$$\begin{aligned}\langle \gamma_{i'j'q}\gamma_{l'm'n}\rangle &= \frac{1}{N_x^2N_y^2} \sum_{a=0}^{N_x-1} \sum_{b=0}^{N_y-1} \sum_{c=0}^{N_x-1} \sum_{d=0}^{N_y-1} \Delta_{abq:cdn} e^{-I2\pi ai'/N_x} e^{-I2\pi bj'/N_y} e^{-I2\pi cl'/N_x} e^{-I2\pi dm'/N_y} \\ &= \frac{1}{N_x^2N_y^2} \sum_{a=0}^{N_x-1} \sum_{b=0}^{N_y-1} \sum_{c=0}^{N_x-1} \sum_{d=0}^{N_y-1} \Delta_{11q:1+(c-a),1+(d-b),n} e^{-I2\pi a(i'+l')/N_x} e^{-I2\pi b(j'+m')/N_y} e^{-I2\pi(c-a)l'/N_x} e^{-I2\pi(d-b)m'/N_y}\end{aligned}$$

$$= \frac{1}{N_x N_y} \sum_{c=0}^{N_x-1} \sum_{d=0}^{N_y-1} \Delta_{11q:1+c,1+d,n} \delta_{i',-l'} \delta_{j',-m'} e^{-I2\pi cl'/N_x} e^{-I2\pi dm'/N_y}. \tag{22}$$

Substituting Eq. (22) for the $\langle \gamma_{i'j'q} \gamma_{l'm'n} \rangle$ in the correlation functions [i.e., Eq. (21)] and summing over l' and m' gives

$$\langle c_{ijk}(t) c_{lmn}(0) \rangle = \frac{1}{N_x N_y} \sum_{i'=0}^{N_x-1} \sum_{j'=0}^{N_y-1} \sum_{c=0}^{N_x-1} \sum_{d=0}^{N_y-1} \sum_{q=1}^{N_z} [e^{\overline{\overline{\Gamma}}_{i'j'}t}]_{kq} \Delta_{11q:1+c,1+d,n} e^{I2\pi i'(i-l)/N_x} e^{I2\pi j'(j-m)/N_y} e^{I2\pi i'c/N_x} e^{I2\pi j'd/N_y}. \tag{23}$$

Defining the quantity

$$D_{i'j'qn} = \frac{1}{N_x N_y} \sum_{c=0}^{N_x-1} \sum_{d=0}^{N_y-1} \Delta_{11q:1+c,1+d,n} e^{I2\pi i'c/N_x} e^{I2\pi j'd/N_y}, \tag{24}$$

Eq. (23) reduces to

$$\langle c_{ijk}(t) c_{lmn}(0) \rangle = \sum_{i'=0}^{N_x-1} \sum_{j'=0}^{N_y-1} \sum_{q=1}^{N_z} [e^{\overline{\overline{\Gamma}}_{i'j'}t}]_{kq} D_{i'j'qn} e^{I2\pi i'(i-l)/N_x} e^{I2\pi j'(j-m)/N_y}. \tag{25}$$

For a given pair of $i'j'$, the diagonalizing transform of $\overline{\overline{\Gamma}}_{i'j'}$ is denoted by $\overline{\overline{R}}^{i'j'}$ and the corresponding matrix elements are $R^{i'j'}_{kn}$. Combining this definition with the transformation in Eq. (16), the expression for the correlation functions [i.e., Eq. (25)] becomes

$$\langle c_{ijk}(t) c_{lmn}(0) \rangle = \sum_{i'=0}^{N_x-1} \sum_{j'=0}^{N_y-1} \sum_{q=1}^{N_z} \sum_{p=1}^{N_z} R^{i'j'}_{kq} e^{\lambda^{i'j'}_q t} R^{\dagger i'j'}_{qp} D_{i'j'pn} e^{I2\pi i'(i-l)/N_x} e^{I2\pi j'(j-m)/N_y}, \tag{26}$$

where the $\lambda^{i'j'}_q$ are the eigenvalues of the matrix $\overline{\overline{\Gamma}}_{i'j'}$. This is the final form of the correlation functions used for computations.

Equation (26) is the basis for fitting the diffusion parameters using a least squares fitting procedure. The value of the objective function [Eq. (8)] can be computed directly using Eq. (26). However, most advanced optimization algorithms require at least the gradients of the objective function with respect to the fitting parameters. The gradients of the correlation functions can be computed analytically and corresponding formulas are given in Appendix A. However, using numerical gradients was found to be substantially faster than analytic gradients for the system sizes explored in this work.

The optimization solver used for fitting is based on the limited memory, variable metric (LMVM) algorithm. This is part of the TAO optimization package [46], which is supplied as part of the PETSC suite of high performance numerical solvers [47,48]. PETSCversion 3.11.1 was used for this work. The LMVM algorithm requires evaluation of the objective function and its gradients. Optimizations were performed using both numerical finite difference gradients and analytic gradients. For the numerical gradients, an increment of 10^{-7} was used. The optimization using numerical gradients was done first and the results were used as a starting point for an optimization using analytic gradients. In general, using analytic gradients had only a minor effect on the fit relative to numerical gradients.

The optimization calculations themselves were run by parallelizing the evaluation of the objective function and, when they are used, analytic gradients. The final values for these quantities were replicated across all processes and the optimizers were run serially. Most of the computationally intensive calculations involve multiple nested loops. The parallelization strategy consisted of unwrapping the outer loops into a single long loop, dividing this into equal segments and assigning each segment to an individual processor, calculating the contributions from each segment independently and then recombining the contributions using either a call to an Allreduce or an Allgather function. This is relatively simple to implement and allows the calculation to be run in parallel without too much difficulty. An optimization on 96 cores using 11 time points could be performed in a little under 2 h using numerical gradients and in about 7 h using analytic gradients.

III. SIMULATION DETAILS

The Lennard-Jones fluid was chosen for testing this approach to extracting spatially dependent transport parameters from a fluid simulation because (1) the Lennard-Jones fluid is well characterized in terms of many of its properties and (2) long simulations can be performed with relatively little effort. The model and parameters used here are the same as those used in a previous study of flow in a microchannel [13].

The nonbonding interaction potential for two Lennard-Jones particles i and j is given by

$$u_{ij}(r_{ij}) = 4\epsilon_{ij}\left[\left(\frac{\sigma_{ij}}{r_{ij}}\right)^{12} - \left(\frac{\sigma_{ij}}{r_{ij}}\right)^{6}\right] + u_0 \qquad \text{if } r_{ij} < r_c$$
$$= 0 \qquad \text{otherwise,}$$

where r_c is a distance cutoff and the parameters ϵ_{ij} and σ_{ij} are the well-depth and hard-sphere radius. The constant u_0 is chosen so that the potential vanishes at the cutoff distance.

For the simple wall-fluid model explored here, there are two types of Lennard-Jones particles. The first represents the

fluid and the second represents particles in the solid material composing the walls. To form the solid, a bond stretching and angle bending interaction are needed. Particles in the solid only interact with each other via the bond stretching and angle bending interactions, there is no Lennard-Jones interaction between solid particles. The bond stretching potential has the form

$$B(r_{ij}) = b(r_{ij} - r_0)^2,$$

where b is the bond stretching parameter and r_0 is the equilibrium bond distance. The angle bending potential between three particles i, j, k is

$$A(\theta_{ijk}) = a(\theta_{ijk} - \theta_0)^2,$$

where a is the angle bending parameter, θ_{ijk} is the angle formed by particles i, j, k with j at the center of the angle, and θ_0 is the equilibrium bond angle (in this case it is chosen to be 90°). The solid material is formed from a simple cubic lattice and bonds only appear between nearest neighbor particles. The angle bend only forms between two particles i and k that are both bonded to particle j at a 90° angle. A particle in the interior of the solid participates in 6 bonds and is the center particle for 12 angle bends.

Lennard-Jones parameters are defined for fluid-fluid and solid-fluid interactions. Two types of system were investigated, a wetting system and a nonwetting system: these differ from each other only in the strength of the solid-fluid interaction. The fluid-fluid interaction was set to $\epsilon_{FF} = 1.0$ and the hard sphere radius for all particles was set to $\sigma_{FS} = \sigma_{FF} = \sigma = 1.0$. For the wetting surface, the solid-fluid interaction was set to $\epsilon_{SF} = 1.0$ (the same as the fluid-fluid interaction) and for the nonwetting system the solid-fluid interaction was set to $\epsilon_{SF} = 0.25$. The stretching and bending parameters for all simulations were $b = 200.0$ and $a = 10.0$ and the equilibrium bond distance was set to $r_0 = 1.0$. The cutoff in all simulations was $r_c = 2.5\sigma$. All particles have the same mass, $m = 1.0$.

The simulation size was chosen to consist of a solid slab consisting of $30 \times 30 \times 9$ particles located in a box of dimension $30.0 \times 30.0 \times 45.0$ (all units are in terms of ϵ, σ, and m). The simulation box extends from $z = -22.5$ to 22.5 and the center of the solid slab is set at $z = -22.5$. Using periodic boundary conditions, approximately half of the slab is located on the other boundary at $z = 22.5$. A channel forms between the two ends of the simulation cell and is filled with 24 276 fluid particles. Combined with the 8100 solid particles, this gives a total of 32 376 particles in the simulation. A simulation of 5×10^5 time steps can be done in a few hours on a system of this size. For a time step of 0.01 in reduced units ($\sqrt{m\sigma^2/\epsilon}$), this corresponds to a simulation of 5×10^3 Lennard-Jones time periods. If the Lennard-Jones fluid were modeling argon [49], which would be expected to be a relatively slowly relaxing liquid, the simulation would be 1078 ns long. This is a long simulation for a realistic molecular fluid using classical potentials (e.g., water between two mineral surfaces), but still within the capabilities of modern simulation codes for a comparable number of particles.

All liquid particles were labeled as belonging to either class "0" or class "1" (the labels have no effect on the physical properties of the particles) with half the particles assigned the label "0" and the other half the label "1." The labels do not effect the trajectories themselves but they provide a mechanism for tracking particle self-diffusion. Concentrations represent the total number of particles with label "1" in a grid cell. All correlation functions represent fluctuations in the value of this concentration variable between different grid cells. A snapshot of the simulation with the overlaid grid and the labeled fluid particles is shown in Fig. 1.

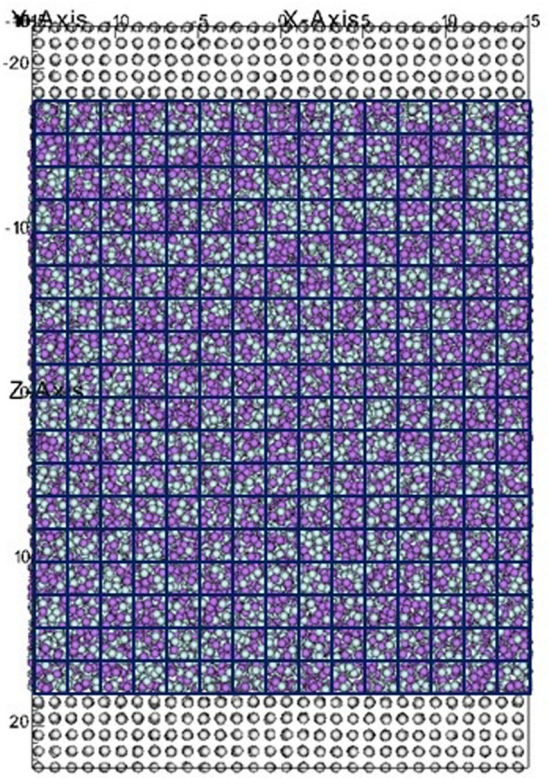

FIG. 1. Snapshot of an MD simulation with overlaid grid. For clarity, the linear dimensions of the grid cells are twice as big as those used in the simulation. Fluid particles are colored purple (dark) and white (light), representing the labels "0" and "1."

The simulations were prepared by equilibrating the system using standard techniques for an extended period. The density at the center of the channel after equilibration was 0.744 for the wetting system and 0.772 for the nonwetting system. The target temperature for the simulations is 0.722. After equilibration, the actual simulations used for collecting data were run as constant energy simulations. For the first step of each simulation, the velocities are randomly reset from a Maxwell-Boltzmann distribution corresponding to the target temperature of 0.722. The average temperature for the simulations was about 0.03 reduced units higher than the target temperature.

The correlation matrix $\tilde{C}_{ijk:lmn}(t)$ was calculated for all adjacent pairs of grid cells (all cells sharing either a face, an edge, or a corner). A list of cell pairs is provided in Table I. Correlation functions for pairs are collected individually during the simulation; these are then averaged in the xy plane before performing the optimization. Displacements parallel to the surfaces are assumed to be equivalent with respect to

TABLE I. Listing of all index pairs used for calculating correlation functions. NN is nearest neighbor, NNN is next-nearest neighbor.

Description	Index pairs
Autocorrelations	$\{ijk : ijk\}$
NN, parallel	$\{ijk : i \pm 1, jk\}, \{ijk : i, j \pm 1, k\}$
NN, perpendicular	$\{ijk : ij, k \pm 1\}$
NNN, parallel	$\{ijk : i \pm 1, j \pm 1, k\}$
NNN, perpendicular	$\{ijk : i \pm 1, j, k \pm 1\}, \{ijk : i, j \pm 1, k \pm 1\}$
Corner	$\{ijk : i \pm 1, j \pm 1, k \pm 1\}$

ordering, so that the correlation function corresponding to the pair $\{ijk : i+1, jk\}$ is equivalent to $\{i+1, jk : i+2, jk\}$. Pairs of correlation functions that can be mapped to each other by 90° rotations in the xy plane were also considered to be equivalent. Displacements in the z direction were not considered to be equivalent and the functions $C_{ijk:ij,k+1}$ were treated separately from $C_{ij,k+1:ijk}$. After averaging, this left approximately $9N_z$ unique correlation functions. The in-plane averaging implied that a minimum of N_xN_y functions contribute to each average and this could potentially be increased by a factor of 4 by rotational symmetry.

Because each correlation function used in the curve fits is an average over many individual functions, the objective function [i.e., Eq. (8)] was modified to

$$\chi(\overline{a}) = \sum_s \sum_{\{i,j\}} w_{ij}([e^{\overline{\overline{L}}(\overline{a})t_\tau} \cdot \overline{\overline{\Delta}}]_{ij} - \tilde{C}_{ij}(t_s))^2, \tag{27}$$

where the w_{ij} are weights that reflect the relative number of individual functions contributing to the averaged function. The weights can easily be calculated as a part of the averaging process.

The correlation functions were sampled once every 100 time steps or, equivalently, once per Lennard-Jones time unit. The density profile for the fluid and solid was also calculated. Based on a preliminary calculation of the density profile, the interface between the solid and liquid phases was determined to be at the values $z = \pm 18.1125$. The number of grid cells in each dimension was chosen to be $N_x = 30$, $N_y = 30$, $N_z = 36$, which leads to nearly cubic cells with all dimensions close to 1.0. The correlation functions were evaluated using a standard sliding window scheme [50] to guarantee that maximal information was extracted from the simulation. Correlation values up to $t = 100$ were collected.

The equilibrium fluctuation matrix $\overline{\overline{\Delta}}$ is given by the value of the correlation functions at time $t = 0$. However, since not all correlation functions are measured, some parts of $\overline{\overline{\Delta}}$ are unknown. If the fluctuating quantities are not conserved, then it is likely that the unmeasured values can be set to zero if the cell pairs are sufficiently far apart. However, for conserved quantities, the equilibrium cross correlations have finite values. This can be seen in a simple case consisting of a box in which a fixed number of particles are distributed, completely at random and with a uniform distribution, over multiple trials. A uniform grid is laid over the box. The total number of particles in the box is fixed, but the number of particles in any grid cell may vary. If we designate the deviation in the number of particles from the average value for a grid cell i as δn_i, then the conservation of particles can be written as

$$\sum_i \delta n_i = 0.$$

Taking the square of this expression and then averaging over all realizations gives

$$\sum_i \langle \delta n_i \delta n_i \rangle + \sum_{i \neq j} \langle \delta n_i \delta n_j \rangle = 0. \tag{28}$$

Because the particles are distributed randomly with a uniform distribution, it follows that the $\langle \delta n_i \delta n_i \rangle$ are all equal. In this example, the particles are noninteracting so given that a grid cell i holds N_i particles, the probability distribution of particles in the remaining grid cells j is the same, no matter what the separation distance is between i and j. It follows that the cross terms in Eq. (28) are all equal. This leads to the relation

$$N_T \langle \delta n_i \delta n_i \rangle + N_T(N_T - 1)\langle \delta n_i \delta n_j \rangle = 0, \tag{29}$$

where N_T is the total number of grid cells. Equation (29) can be solved easily to write the equilibrium autocorrelations in terms of the cross correlations. Since the autocorrelations must be positive, the cross correlations are negative and smaller by a factor of $1/(N_T - 1)$.

Equation (29) suggests a way of approximating the unmeasured elements of $\overline{\overline{\Delta}}$. The sum of all matrix elements in $\overline{\overline{\Delta}}$ must be equal to zero. If the unmeasured values represent grid cells that are separated from each other by a reasonable amount, the value of the cross fluctuations can be assumed to be the same for all unmeasured correlations and this value can be determined by solving the equation

$$\sum_{\{i,j\}} (\overline{\overline{\Delta}})_{ij} + (N_T - N_M)\langle \delta n_i \delta n_j \rangle = 0$$

for $\langle \delta n_i \delta n_j \rangle$, where N_M is the total number of measured values. If the minimal separation distance of the unmeasured grid cells is large enough, then it is likely that the effects of any local structuring will have died out and the assumption that the unmeasured values are the same will be increasingly accurate. In these simulations, the minimal separation is one grid cell.

IV. RESULTS AND DISCUSSION

A. Density and diffusion coefficients

The wetting and nonwetting surfaces investigated in this paper produce different profiles for the liquid density near the walls. The density profiles are shown in Figs. 2 and 3. The wetting system (Fig. 2) shows a highly oscillatory profile that is rapidly damped with increasing distance from the solid surface, while the nonwetting system (Fig. 3) shows much weaker oscillations that appear to be superimposed on a monotonically increasing density profile. Both profiles show a distinct gap between the fluid density and solid density where the density is very close to zero, making it possible to define the fluid-solid interface fairly precisely. The location of the fluid-solid interface at $z = \pm 18.1125$ is based on this gap and is limited in resolution by the size of the bins used to calculate the density profile. The boundary region extends about 5σ

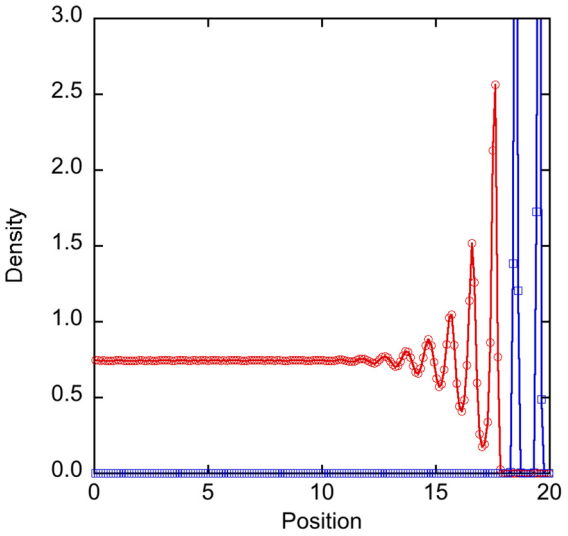

FIG. 2. Density profile of liquid (red circles) and solid (blue squares) phases as a function of z for a wetting surface. Position is measured in units of σ. Only half of the channel is shown due to symmetry.

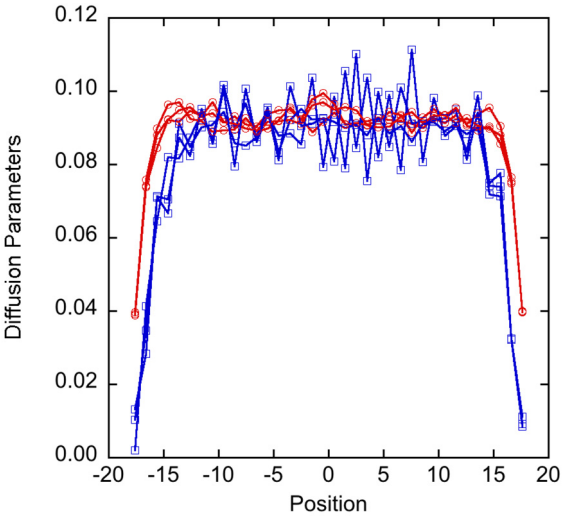

FIG. 4. Diffusion parameters α (red circles) in the parallel direction and β (blue squares) in the perpendicular direction for the wetting system as a function of position z. The results of three independent simulations are shown.

from the wall for the wetting system and about 4σ for the nonwetting system.

The correlation functions were calculated at intervals of 1.0 Lennard-Jones time units up to a maximum time of 100.0 but not all points were used in the fit. Both low sampling fits, using every 10th point, and high sampling fits, using every second point, were performed. The low sampling fits required much less computation to evaluate the objective function and also appeared to weigh the short time behavior of the correlation functions less heavily than the higher sampling fits. This is important since the proposed functional form of the diffusion operator, Eq. (11), does not show desirable performance in capturing the short time behavior of the correlation functions seen in the simulations.

Plots of the α and β components of the diffusion tensor as a function of z from the low sampling fits are shown in Figs. 4 and 5 for the wetting and nonwetting systems. To demonstrate the uncertainties, the results of three separate simulations are shown. The curves should also be symmetric about $z = 0$ and this can also be used to assess uncertainty. Both the wetting and nonwetting systems show variations in the diffusion tensor near the solid-liquid boundaries, although the curves exhibit a significant amount of noise. For the wetting system, both components of the diffusion tensor drop off substantially near the boundary, with the perpendicular component (β)

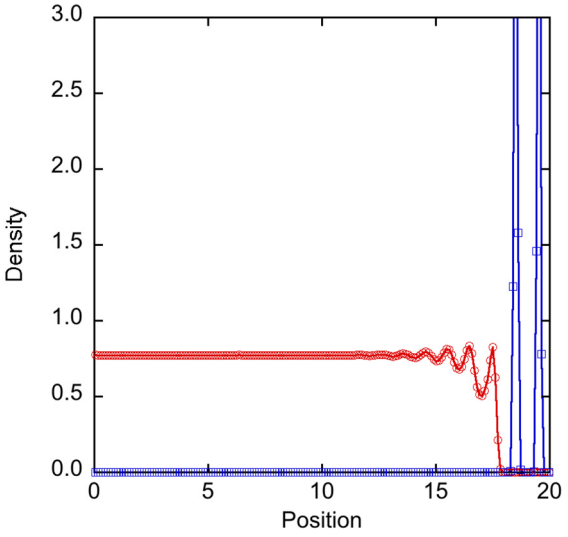

FIG. 3. Density profile of liquid (red circles) and solid (blue squares) phases as a function of z for a nonwetting surface. Position is measured in units of σ. Only half of the channel is shown due to symmetry.

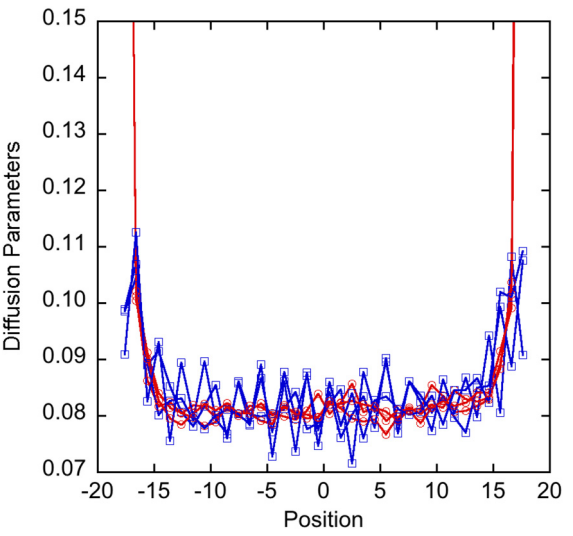

FIG. 5. Diffusion parameters α (red circles) in the parallel direction and β (blue squares) in the perpendicular direction for the nonwetting system as a function of position z. The results of three independent simulations are shown.

showing a larger drop. This is in accord with the density plot in Fig. 2, which suggests much more structuring of the fluid near the boundary. This result is similar to what was seen in studies by Simonnin *et al.* [18] and Marry *et al.* [25] that exhibited lower values of the self-diffusion coefficient in the vicinity of a clay-water boundary. Although no quantitative assessment of ordering in the plane parallel to the surface was made in our simulations, it is likely that such ordering is less extensive than ordering perpendicular to the surface. This may account for the asymmetry between the two components.

The results for the nonwetting system also show deviations from bulk behavior near the boundary. However, these are the opposite of the deviations seen for the wetting system. Instead of decreasing near the boundary, both components of the diffusion tensor increase. This can also be rationalized in terms of the density profile; the decreased fluid density near the solid would lead to the corresponding increase in the self-diffusion constant (i.e., "rarefied" effects). Both components of the diffusion tensor also have roughly the same values, except for the cells immediately adjacent to the boundary, which is compatible with the relatively minimal structuring of the fluid near the boundary. This behavior is in accordance with simulations of the vapor-liquid interface of water by Liu *et al.* [24]; the vapor-liquid interface resembles the nonwetting Lennard-Jones interface with respect to a decrease in fluid density near the surface.

Although these plots are qualitatively appealing, they are not quantitative. To check the accuracy of these fits, the self-diffusion coefficient in the center of the system was calculated by selecting all particles in a slab 1.0 σ units wide in the center of the system at $t = 0$ and calculating their mean square displacements for 20.0 Lennard-Jones time units. At the end of this period, a new set of particles from this band was selected and followed for another 20.0 time units. This calculation was repeated until the end of the simulation and results from all individual trajectories were combined into single curves for diffusion in the parallel and perpendicular directions. Only particles from the center of the system were selected as these were expected to remain in a region of uniform density over the 20.0 time unit interval.

The mean square displacements in the direction parallel and perpendicular to the surface are shown in Fig. 6 for the wetting and nonwetting systems. The plots are normalized so that the slope is equal to the diffusion coefficient. Both the parallel and perpendicular components of diffusion are almost identical, which matches the observation that the density profiles are quite flat in the center of the channel and hence would be expected to be isotropic. The diffusion coefficient for the wetting system ($\approx$0.065) is a bit higher than for the nonwetting system ($\approx$0.056), which again matches the observation that the density in the center of the nonwetting system is slightly higher than for the wetting system. Because the density at the center of the simulation cell is constant over an extended region and the displacements measured over the period of 20.0 time units are small (less than 2σ), the displacements are taken as representing the true value of the diffusion coefficient in the center of the channel. The fitted values of α and β in the center of the channel are about 0.09 and 0.08 for the wetting and nonwetting systems, respectively. This is close to a 50% error relative to the previously noted values of

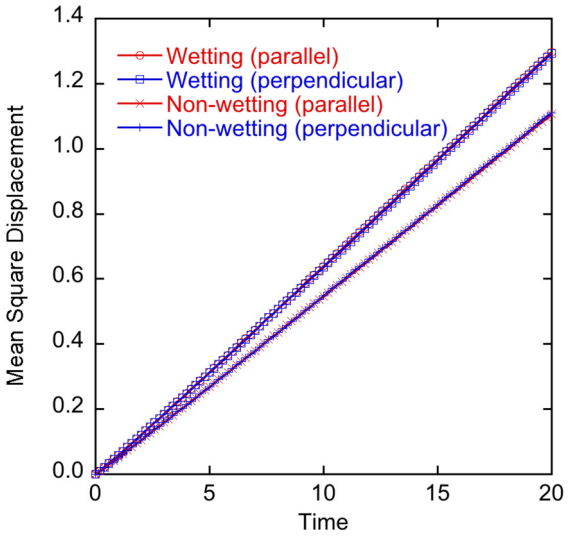

FIG. 6. Mean square displacement as a function of time in the directions parallel and perpendicular to the surface for both the wetting and nonwetting systems. The plots have been scaled so that the slope is equal to the diffusion constant.

0.065 and 0.056. For comparison, previous work on the simple 1D problem [38] had the advantage that, by construction, the proposed diffusion equation was an accurate description of the underlying dynamics; the fit was able to reproduce the spatially varying diffusion coefficient almost identically. However, for the current system, it appears that a diffusion equation with a spatially varying diffusion coefficient is not sufficient.

B. Analysis of correlation functions

The errors in the diffusion coefficients can be better understood by comparing the correlation functions measured from the simulations with correlation functions generated from Eq. (6) using the operator $\overline{\overline{L}}$ based on the fitted values of the α and β. The correlations coming from the simulation are of interest in themselves and clearly show the influence of fluid structure on transport in the neighborhood of the surface. Figure 7 compares grid cell autocorrelation functions from both the simulation and the fits for grid cells immediately adjacent to the boundary and at the center of the channel [note that autocorrelation functions correspond to $C_{ijk:ijk}(t)$]. The relaxation of the grid cells close to the boundary is much slower than for grid cells in the center of the system. It is also clear that the fitted correlation functions, while qualitatively similar to the simulations, have significant quantitative differences. In particular, the fitted functions relax much more slowly than the simulations at shorter times. Conversely, the simulations appear to relax more slowly at longer times, at least near the surface. The faster relaxation of the fitted correlation functions at longer times is consistent with an overestimation of the diffusion coefficient by the fitting procedure. The differences between the fitted forms and the simulations appear to reflect deficiencies in the assumed form of the diffusion equation at short timescales and length scales and not a failure to capture behavior due to confinement of the fluid. For comparison, the

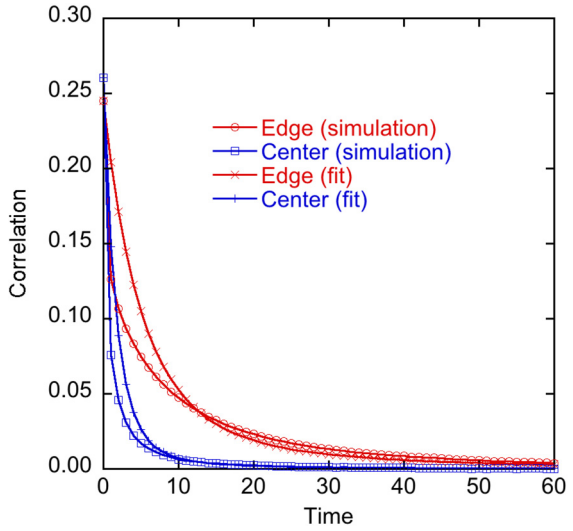

FIG. 7. Autocorrelation functions as function of time for a cell at the edge (i.e., adjacent to the boundary) of the system and a cell in the center. Plots for both original simulation data and calculations from low sampling fits are shown.

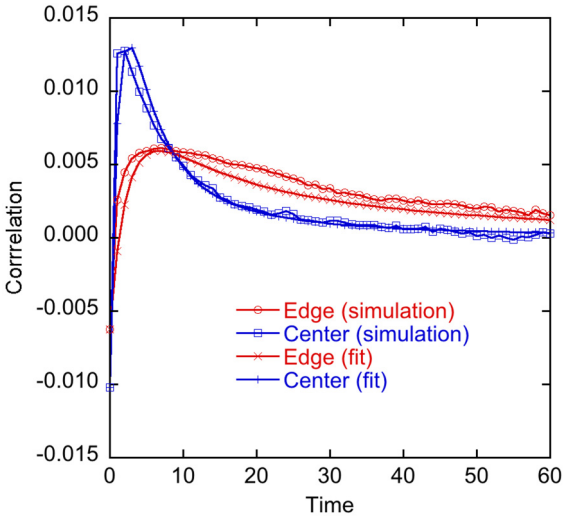

FIG. 9. Correlation functions between nearest neighbors in the direction perpendicular to the surface as a function of time for cells at the edge of the system and cells in the center. Plots for both original simulation data and calculations from low sampling fits are shown.

simulation of a purely periodic system with no solid boundary showed that the correlation functions for the periodic system very closely match the correlation functions calculated at the center of the confined channel.

Similar behavior is seen for correlation functions of the nearest neighbors in the parallel and perpendicular directions. Plots of these correlation functions are shown in Figs. 8 and 9. Note that the response for these cross-correlation functions between different grid cells is about an order of magnitude smaller than the response of corresponding autocorrelation functions. Both plots show behavior that qualitatively resembles Fig. 7 with respect to the comparison between simulation and the fits. The short time response is faster for the simulations and the longer time decay seems faster for the fits. This suggests that the proposed evolution operator represented by Eq. (11) lacks some essential physics despite the flexibility to use different values of the diffusion tensor at each value of z.

For the low sampling fit, the first value of the correlation function that actually influences the fit is at $t = 10.0$ (the value at $t = 0$ is completely determined by the fluctuation matrix $\overline{\overline{\Delta}}$), so the short time behavior is not contributing to the values of the diffusion tensor. For the higher sampling fits, where the interval between sampling points is 2.0, the short time behavior is expected to have a much bigger influence on the optimization and this indeed appears to be the case. Plots of the diffusion tensor for the wetting and nonwetting

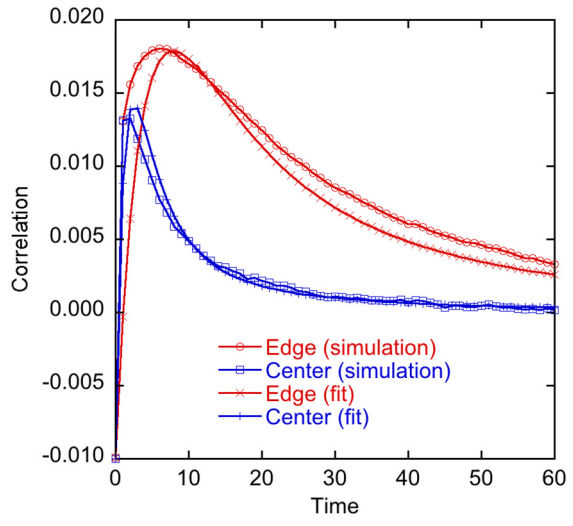

FIG. 8. Correlation functions between nearest neighbors in the direction parallel to the surface as a function of time for cells at the edge of the system and cells in the center. Plots for both original simulation data and calculations from low sampling fits are shown.

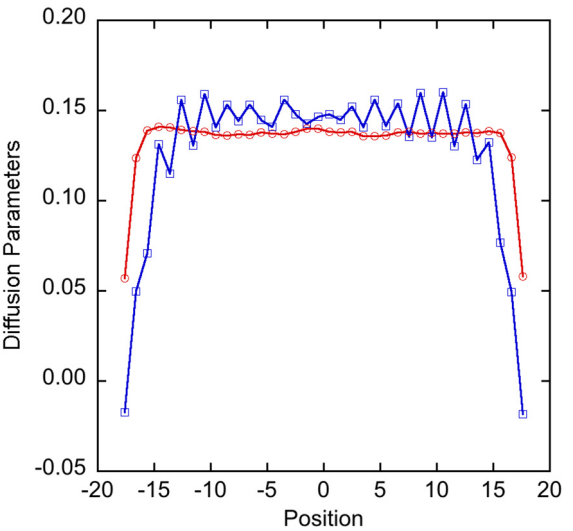

FIG. 10. Diffusion parameters α (red circles) and β (blue squares) for the wetting system as a function of position from high sampling fits. Only the fit from a single simulation is shown.

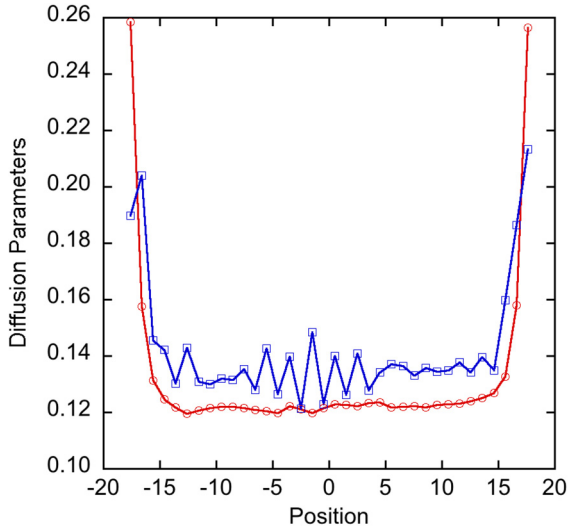

FIG. 11. Diffusion parameters α (circles) and β (squares) for the nonwetting systems as a function of position from high sampling fits. Only the fit from a single simulation is shown.

systems are shown in Figs. 10 and 11, respectively, for the high sampling fits.

The most striking difference between the high and low sampling fits is a sharp increase in the diffusion coefficients at the center of the channel when more points are included. There also appears to be a slight separation between the α and β values in the center of the channel, particularly with respect to the nonwetting system. Based on the mean square displacement calculations, this would not be physical. Figure 12 compares the autocorrelation functions calculated from the low and high sampling fits with the simulation results for the wetting system. It can be seen that the high sampling fit results in a faster response at short times but also appears to result in a poorer fit at medium to longer times. Plots of other correlation

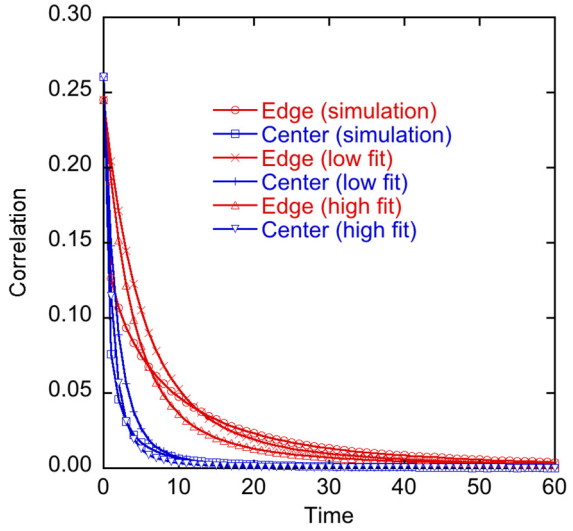

FIG. 12. Comparison of low and high sampling fits for the autocorrelation functions for the wetting system. The original simulation results are also included.

functions show similar behavior. This suggests that a good functional form will be important in correctly modeling the response over the entire range of timescales. The current form does not handle the behavior at short timescales well and probably distorts the fit to the longer times by trying to fit the large amplitude responses at short times. The extent to which this happens is controlled by the number of fitting points, hence the variability between fits depending on the number of sampling points. This would not be a critical problem if the target function was capable of reproducing the observed behavior more exactly and adding additional points would not have a large effect on the results. An extreme case would be a fitting form that can *exactly* match the data (which is assumed to be noise free). In this case, additional points would fall on the existing fit and their contribution to the objective function would be zero.

C. Implementation of memory function

A simple extension was made to the diffusion model in an attempt to improve the agreement between the fits and simulation. The constitutive relation for the diffusive flux was modified to include a memory function. The new constitutive relation is of the form

$$\vec{j}_c = -\int_0^t \phi(t-t')\overline{\overline{D}}(\vec{r})\cdot\nabla(\vec{r})dt', \tag{30}$$

where $\vec{j}_c$ is the concentration flux and $\phi(t)$ is a position-independent memory kernel. A simple exponential decay was chosen for $\phi(t)$,

$$\phi(t) = \frac{e^{-t/\tau}}{\tau}, \tag{31}$$

where τ denotes a characteristic correlation time constant for the memory kernel. Numerical details are given in Appendix B, but the equations are only slightly more complicated than the formalism described in Sec. II. The fits were modified to include τ as an additional parameter and all fits were performed using analytic gradients.

Although inclusion of a memory kernel has considerably improved fits to correlation functions in other contexts, the benefits were relatively minimal in this case. For both wetting and nonwetting systems, changes resulting from inclusion of the memory kernel are small, as shown in Figs. 13 and 14. The only improvement is that the slight difference between α and β in the center of the systems appears to be diminished. However, the differences between the fitted diffusion coefficients in the center of the gap and the values measured from mean square displacement still remain.

In addition, the effect of the memory kernel on the correlation functions calculated from the fits is also small. A comparison of the nearest neighbor correlation functions in the perpendicular direction is shown in Fig. 15 for the wetting system. The figure includes correlation functions calculated from the high sampling fits with and without the memory kernel, as well as the original simulation results. This set of correlation functions was chosen because the differences are large enough to be seen easily on a graph; for most other curves the differences between functions calculated with and without the memory kernel are minute. Both sets of

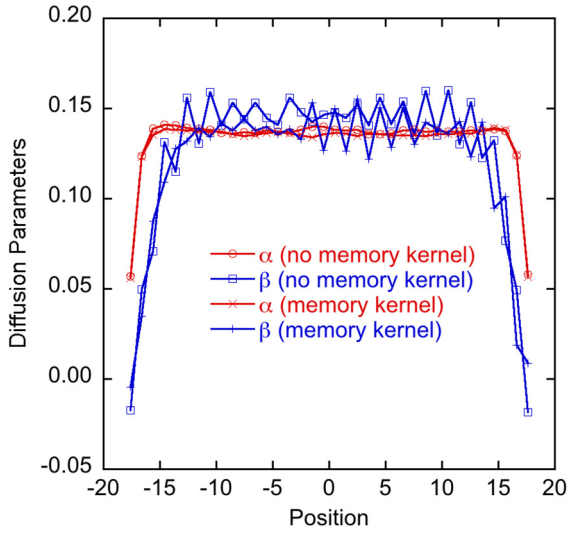

FIG. 13. Comparison of diffusion parameters calculated with and without the memory kernel for the wetting system. Both fits used a high sampling of time points. Only the fits from a single simulation are shown.

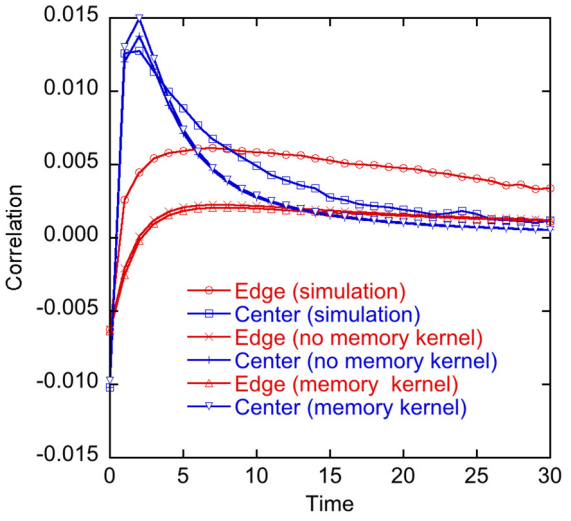

FIG. 15. Comparison of the nearest neighbor correlation functions in the direction perpendicular to the surface for the wetting system calculated with and without the memory kernel. The original simulation results are also included.

fitted curves are almost identical. The remaining correlation functions for both wetting and nonwetting systems also show very little change. The fitted values of the time constant τ for the wetting and nonwetting systems are 0.108 and 0.157, respectively, implying that the effect of the memory kernel decays fairly quickly. In a prior study, the inclusion of the memory kernel in fits to correlation functions used to calculate the shear viscosity had two effects [44]. The first was that it converted the fitting function from a pure exponential decay into a function with zero slope at $t = 0$. The correlation functions calculated from grid cells have a finite slope at $t = 0$, most likely because the concentration in each grid cell is a piecewise constant function of time instead of smoothly varying. Forcing the slope to vanish at $t = 0$ has the result of enhancing the correlation at short times, which is the opposite of what is needed here. (On the scale of the plots shown here, this effect is negligible.) The second effect of including a memory kernel was to enable the possibility of creating exponentially damped oscillations at longer times. Again, this is not a behavior that is seen in the simulations in this study.

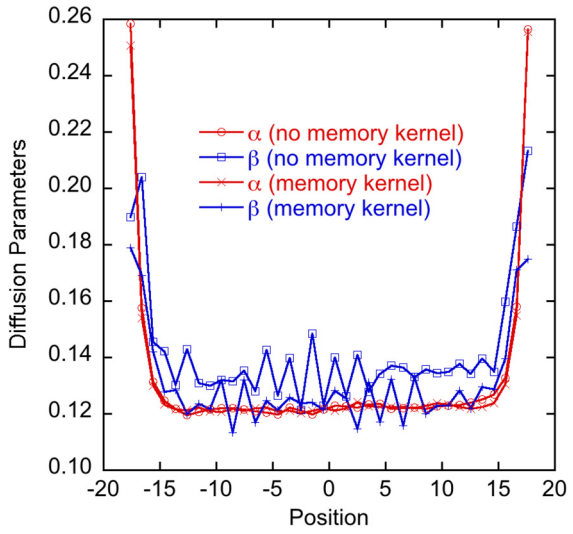

FIG. 14. Comparison of diffusion parameters calculated with and without the memory kernel for the nonwetting system. Both fits used a high sampling of time points. Only the fits from a single simulation are shown.

V. CONCLUSIONS

We investigated the utility of using correlation functions formed by projecting hydrodynamic fields onto the cells of a structured grid to determine spatially varying transport parameters. Correlation functions were calculated from simulations of a simple Lennard-Jones fluid in a channel configuration and used as the inputs to fits of a diffusion equation with a spatially varying and nonisotropic diffusion tensor. The fitted values of the diffusion tensor match qualitative expectations of the behavior of the fluid based on the behavior of the density profile but are not quantitative, based on comparison with direct calculations of the diffusion constant in the center of the channel. Nevertheless, the results demonstrate the following:

(i) The fits are possible and lead to physically plausible results. The correlation functions can be calculated in a reasonable amount of time and the fitted values themselves have small enough uncertainties that physical behavior of interest can be discerned. The method can be easily applied to more complicated models of liquids (e.g., water confined by two mineral interfaces). All that is needed is to label the liquid molecules, evaluate the concentration of labeled molecules in an overlaid grid, and calculate the correlation functions between grid cells.

(ii) Generalizing the diffusion equation to include spatial variation and anisotropy of the diffusion tensor is not sufficient to fully model diffusive behavior in a small channel. The primary support for this conclusion is the comparison of

the correlation functions calculated from the fitted diffusion equation and the correlation functions calculated directly from the simulations. The inability to capture the full dynamics results in relatively poor values for the diffusion parameters compared to direct calculation from mean square displacements.

(iii) Incorporating a simple memory kernel in the diffusion constitutive relation results in some improvement but is not sufficient to provide a quantitative model for transport in these systems.

The second conclusion is important since it shows that this approach to fitting molecular simulation behavior to continuum equations may serve both to provide direction on what kinds of coarse-grained equations are needed in order to model flows at the nanometer scale while also giving guidance on the failings of existing equations.

As noted, incorporating a simple memory kernel into the constitutive relation does not result in a substantial improvement in the fitted functions. Other potential improvements are to generalize the constitutive equation for the diffusive flux to a nonlocal form or to couple the diffusion equation to the microscopic velocity field due to fluctuations. The diffusion equation in the presence of a velocity field ($\vec{v}$) is

$$\frac{\partial c}{\partial t} + \nabla \cdot (\vec{v}c) = \nabla \cdot \overline{\overline{D}} \cdot \nabla c. \tag{32}$$

Considering fluctuating terms for both velocity field and concentrations (i.e., $\vec{v} = \vec{v}_0 + \delta\vec{v}$ and $c = c_0 + \delta c$) and expanding Eq. (32) to first order in fluctuating quantities leads to

$$\frac{\partial \delta c}{\partial t} + c_0 \nabla \cdot \delta\vec{v} + \vec{v}_0 \cdot \nabla \delta c = \nabla \cdot \overline{\overline{D}} \cdot \nabla \delta c. \tag{33}$$

For a system in equilibrium, $\vec{v}_0$ vanishes, implying that only divergent flows are capable of contributing to diffusive transport. Divergent flows [i.e., compressible flows or $\nabla \cdot (\rho\vec{v}) \neq 0$] result in changes in the density (such as those for longitudinal sound waves) and this further implies that, in addition to modeling velocity fields at the nanoscale, the energy equation also needs to be considered. The inclusion of both the energy and momentum equations in the model represents a major increase in complexity, but it also offers considerable opportunity for studying new behavior. Alternatively, the $c_0 \nabla \cdot \delta\vec{v}$ term could be viewed as a random fluctuation driving the diffusion equation, leading to a fluctuating hydrodynamics expression. However, in this case the autocorrelation function for the fluctuation is unlikely to be well represented by a delta function, which is a typical assumption.

It is also possible that at molecular length scales the motion of particles is simply not diffusive or contains important nondiffusive components. This could result in governing equations containing integrodifferential operators or possibly higher order terms, provided they can be added in a justifiable way that does not violate basic consistency and conservation conditions. Incorporating these kinds of terms will result in more complicated theories, but also provides opportunities for identifying new behavior.

ACKNOWLEDGMENTS

This work was supported by the Laboratory Directed Research and Development Program at PNNL. G.K.S. and C.J.M. were supported by the US Department of Energy (DOE), Office of Science, Office of Basic Energy Sciences, Division of Chemical Sciences, Geosciences and Biosciences. J.F.M. was partially supported by National Science Foundation (NSF) Grant No. 1916879. PNNL is a multiprogram national laboratory operated for DOE by Battelle under Contract No. DE-AC05-76RL01830.

APPENDIX A: ANALYTIC GRADIENTS

Analytic gradients of the objective function can be obtained for the reduced problem formulation by making use of the Laplace transform on the time evolution operators. For the systems investigated in this paper, the analytic gradients actually take more time to calculate than numerical gradients (by a factor of about 4), but for completeness, the derivation of the gradients is included here. For more complicated systems, it may prove that analytic gradients are more efficient.

The gradients of the operators $\overline{\overline{\Gamma}}_{ij}$ with respect to the parameters of the diffusion matrix can be written as

$$\frac{\partial \Gamma^{ij}_{kk}}{\partial \alpha_m} = \left\{ \frac{1}{\Delta x^2}\left[2\cos\left(\frac{2\pi i}{N_x}\right) - 2\right] + \frac{1}{\Delta y^2}\left[2\cos\left(\frac{2\pi j}{N_y}\right) - 2\right]\right\}\delta_{km},$$

$$\frac{\partial \Gamma^{ij}_{kk}}{\partial \beta_m} = -(\delta_{m,k+1} + \delta_{mk})\frac{1}{2\Delta z^2}(1 - \delta_{kN_z}) - (\delta_{m,k-1} + \delta_{mk})\frac{1}{2\Delta z^2}(1 - \delta_{k1}),$$

$$\frac{\partial \Gamma^{ij}_{k,k+1}}{\partial \beta_m} = (\delta_{m,k+1} + \delta_{mk})\frac{1}{2\Delta z^2}(1 - \delta_{kN_z}),$$

$$\frac{\partial \Gamma^{ij}_{k,k-1}}{\partial \beta_m} = (\delta_{m,k-1} + \delta_{mk})\frac{1}{2\Delta z^2}(1 - \delta_{k1}).$$

All other pairs vanish. The remaining step is to calculate the gradients of the correlation functions in terms of the gradients of $\overline{\overline{\Gamma}}_{ij}$. From the expression for the correlation function, we can write

$$\frac{\partial \langle c_{ijk}(t_s)c_{lmn}(0)\rangle}{\partial a} = \sum_{i'=0}^{N_x-1}\sum_{j'=0}^{N_y-1}\sum_{q=1}^{N_z}\frac{\partial}{\partial a}[e^{\overline{\overline{\Gamma}}_{i'j't_s}}]_{kq}D_{i'j'qn}e^{I2\pi i'(i-l)/N_x}e^{I2\pi j'(j-m)/N_y}.$$

Applying a Laplace transform to the exponentiated operator leads to the expression [51]

$$\nabla_a e^{\overline{\overline{\Gamma}}_{i'j't_s}} = \frac{1}{2\pi I}\oint \overline{\overline{R}}_{i'j'}\cdot\frac{1}{z-t_s\overline{\overline{\Lambda}}_{i'j'}}\cdot\overline{\overline{R}}^{\dagger}_{i'j'}t_s\nabla_a\cdot\overline{\overline{\Gamma}}_{i'j'}\cdot\overline{\overline{R}}_{i'j'}\cdot\frac{1}{z-t_s\overline{\overline{\Lambda}}_{i'j'}}\cdot\overline{\overline{R}}^{\dagger}_{i'j'}e^z dz.$$

Explicitly writing this as a sum over indices gives the equation

$$\begin{aligned}[\nabla_a e^{\overline{\overline{\Gamma}}_{i'j't_s}}]_{kq} &= \frac{t_s}{2\pi I}\sum_{lmnopr}\oint R^{i'j'}_{kl}\frac{1}{z-t_s\lambda_m}\delta_{lm}R^{\dagger i'j'}_{mn}(\nabla_a\overline{\overline{\Gamma}}_{i'j'})_{no}R^{i'j'}_{op}\frac{1}{z-t_s\lambda_p^{i'j'}}\delta_{pr}R^{i'j'}_{rq}e^z dz\\ &= \frac{t_s}{2\pi I}\sum_{mnor}\oint R_{km}\frac{1}{z-t_s\lambda_m^{i'j'}}R^{\dagger i'j'}_{mn}(\nabla_a\overline{\overline{\Gamma}}_{i'j'})_{no}R^{i'j'}_{or}\frac{1}{z-t_s\lambda_r^{i'j'}}R^{\dagger i'j'}_{rq}e^z dz.\end{aligned}$$

Define the matrix of contour integrals as

$$\Phi^{i'j'}_{mr}(t_s) = \frac{t_s}{2\pi I}\oint\frac{1}{\left(z-t_s\lambda_m^{i'j'}\right)\left(z-t_s\lambda_r^{i'j'}\right)}e^{zt_s}dz. \tag{A1}$$

The contour integrals can be evaluated analytically to obtain [52]

$$\begin{aligned}\frac{1}{2\pi I}\oint\frac{1}{(z-t_s\lambda_k)(z-t_s\lambda_l)}e^z dz &= \frac{e^{t_s\lambda_k}-e^{t_s\lambda_l}}{t_s(\lambda_k-\lambda_l)}, \qquad \lambda_k\neq\lambda_l\\ &= e^{t_s\lambda_k} \qquad \lambda_k=\lambda_l.\end{aligned}$$

The gradient of the evolution operator can now be written out explicitly as the multiple sum

$$[\nabla_a e^{\overline{\overline{\Gamma}}_{i'j't_s}}]_{kq} = \sum_{mnor}R^{i'j'}_{km}R^{\dagger i'j'}_{mn}\Phi^{i'j'}_{mr}[\nabla_a\overline{\overline{\Gamma}}_{i'j'}]_{no}R^{i'j'}_{or}R^{\dagger i'j'}_{rq}.$$

Further define the quantity

$$\Psi^{i'j'(a)}_{mr} = \sum_{no}R^{\dagger i'j'}_{mn}\left[\nabla_a\overline{\overline{\Gamma}}_{i'j'}\right]_{no}R^{i'j'}_{or}$$

and the gradient reduces to

$$[\nabla_a e^{\overline{\overline{\Gamma}}_{i'j't_s}}]_{kq} = \sum_{mr}R^{i'j'}_{km}\Phi^{i'j'}_{mr}(t_s)\Psi^{i'j'(a)}_{mr}R^{\dagger i'j'}_{rq}. \tag{A2}$$

The largest array in this equation is $\Psi^{i'j'(a)}_{mr}$, which contains approximately $2N_z^3N_xN_y$ elements. The computation of this structure is of the same order since the gradients of $\overline{\overline{\Gamma}}_{i'j'}$ only contain a maximum of seven nonzero elements so the sum over n and o only contains a few terms. The remaining arrays in Eq. (A2) are all smaller.

APPENDIX B: MEMORY KERNEL

Including the memory kernel in the constitutive relation for the diffusive flux modifies the discretized transport equation to

$$\frac{d\overline{X}}{dt} = \int_0^t\phi(t-t')\overline{\overline{L}}\cdot\overline{X}dt'. \tag{B1}$$

The Laplace transform of Eq. (B1) is

$$\overline{X}(z) = \frac{1}{z-\phi(z)\overline{\overline{L}}}\cdot\overline{X}(t=0). \tag{B2}$$

The Laplace transform of the memory kernel [i.e., Eq. (31)] is

$$\phi(z) = \frac{1}{z\tau+1}. \tag{B3}$$

Combining Eqs. (B2) and (B3) and making use of the diagonalization transform yields the expression

$$\begin{aligned}\overline{X}(z) &= \left[\frac{z+1/\tau}{z^2+z/\tau-\overline{\overline{L}}/\tau}\right]\cdot\overline{X}(t=0)\\ &= \overline{\overline{R}}\cdot\left[\frac{z+1/\tau}{z^2+z/\tau-\overline{\overline{\Lambda}}/\tau}\right]\cdot\overline{\overline{R}}^{\dagger}\cdot\overline{X}(t=0).\end{aligned} \tag{B4}$$

The only modification needed to evaluate the real-time equivalent of this expression is to replace the exponentials of the eigenvalues in expressions like Eq. (16) with the real-time equivalent of the term in square brackets in Eq. (B4). This can be evaluated fairly easily.

For a given eigenvalue λ_i, define the two roots of the expression

$$z^2+z/\tau-\lambda_i/\tau$$

as $\lambda_i^{\pm}$. The inverse Laplace transform of the function

$$\frac{z+1/\tau}{z^2+z/\tau-\lambda_i/\tau}$$

is the function [52]

$$\phi_i(t) = \frac{\lambda_i^+ e^{\lambda_i^+ t}-\lambda_i^- e^{\lambda_i^- t}}{\lambda_i^+-\lambda_i^-}-\frac{1}{\tau}\frac{e^{\lambda_i^+ t}-e^{\lambda_i^- t}}{\lambda_i^--\lambda_i^+}. \tag{B5}$$

Calculating the correlation functions with the memory kernel can be accomplished by substituting Eq. (B5) for the corresponding $\exp(-\lambda_i t)$ in Eq. (26). The gradient of the correlation functions with respect to τ can be evaluated by taking the gradient of Eq. (B5) with respect to τ and substituting $\partial\phi_i(t)/\partial\tau$ for the $\exp(-\lambda_i t)$ in Eq. (26). For the parameter τ, the numerical gradients appeared to be particularly sensitive to the value of the increment, so analytic derivatives with respect to τ were used even if numerical derivatives were used for α and β.

The analytic gradients of the correlation functions with the memory kernel with respect to the diffusion parameters can be evaluated by replacing the right-hand side of the definition of the matrix $\Phi_{mr}^{i'j'}(t_s)$ in Eq. (A1) with the expression

$$\frac{t_s}{2\pi I}\oint\frac{1}{\tau}\frac{z+1/\tau}{\left(z^2+z/\tau-\lambda_m^{i'j'}/\tau\right)\left(z^2+z/\tau-\lambda_r^{i'j'}/\tau\right)}e^{zt_s}dz. \tag{B6}$$

The inverse Laplace transforms for $m\neq r$ can be evaluated by making use of identities of the form

$$\frac{z}{(z-a)(z-b)(z-c)(z-d)} = \frac{A}{z-a}+\frac{B}{z-b}+\frac{C}{z-c}+\frac{D}{z-d}.$$

Collecting all the terms on the right-hand side over a common denominator and equating the coefficients of the powers of z in the numerator to the corresponding terms on the left-hand side yields a set of linear equations. These can then be solved for A, B, C, D using a symbolic manipulation program such as MATHEMATICA [53]. The inverse Laplace transforms of the terms on the right-hand side of Eq. (B6) are readily available and can be easily evaluated once the coefficients A, B, C, D are known. The roots of the quadratic expressions appearing in Eq. (B6) can be mapped to the constants a, b, c, d. This approach is easily extended to the other term appearing in Eq. (B6) by replacing z with 1. The case $m=r$ can be evaluated similarly, except that the identities are of the form

$$\frac{z}{(z-a)^2(z-b)^2} = \frac{A}{(z-a)^2}+\frac{B}{z-a}+\frac{C}{(z-b)^2}+\frac{D}{z-b}.$$

Again, the Laplace transforms of the terms on the right-hand side are readily available.

[1] A. J. Grodzinsky, *Fields, Forces, and Flows in Biological Systems* (Garland Science, London, 2011).

[2] F. Zamani, A. Ullah, E. Akhondi, H. J. Tanudjaja, E. R. Cornelissen, A. Honciuc, A. G. Fane, and J. W. Chew, Impact of the surface energy of particulate foulants on membrane fouling, J. Membr. Sci. **510**, 101 (2016).

[3] J. Chmiola, G. Yushin, Y. Gogotsi, C. Portet, P. Simon, and P.-L. Taberna, Anomalous increase in carbon capacitance at pore sizes less than 1 nanometer, Science **313**, 1760 (2006).

[4] Y. Wang, C. Bryan, H. Xu, and H. Gao, Nanogeochemistry: Geochemical reactions and mass transfers in nanopores, Geology **31**, 387 (2003).

[5] Q. Cao and R. R Netz, Anomalous electrokinetics at hydrophobic surfaces: Effects of ion specificity and interfacial water structure, Electrochim. Acta **259**, 1011 (2018).

[6] N. Schwierz, D. Horinek, and R. R Netz, Anionic and cationic hofmeister effects on hydrophobic and hydrophilic surfaces, Langmuir **29**, 2602 (2013).

[7] I. Kalcher, J. C. F. Schulz, and J. Dzubiella, Electrolytes in a nanometer slab-confinement: Ion-specific structure and solvation forces, J. Chem. Phys. **133**, 164511 (2010).

[8] P. Loche, C. Ayaz, A. Schlaich, D. J. Bonthuis, and R. R. Netz, Breakdown of linear dielectric theory for the interaction between hydrated ions and graphene, J. Phys. Chem. Lett. **9**, 6463 (2018).

[9] A. Bakhshandeh, D. Frydel, A. Diehl, and Y. Levin, Charge Regulation of Colloidal Particles: Theory and Simulations, Phys. Rev. Lett. **123**, 208004 (2019).

[10] D. Kim and E. Darve, Molecular dynamics simulation of electro-osmotic flows in rough wall nanochannels, Phys. Rev. E **73**, 051203 (2006).

[11] Y. Li, J. Xu, and D. Li, Molecular dynamics simulation of nanoscale liquid flows, Microfluid Nanofluid **9**, 1011 (2010).

[12] A. Prakash, J. Pfaendtner, J. Chun, and C. Mundy, Quantifying the molecular-scale aqueous response to the mica surface, J. Phys. Chem. C **121**, 18496 (2017).

[13] B. Palmer, Direct simulation of hydrodynamic relaxation in microchannels, J. Chem. Phys. **109**, 196 (1998).

[14] D. J. Bonthuis and R. R. Netz, Beyond the continuum: How molecular solvent structure affects electrostatics and hydrodynamics at solid–electrolyte interfaces, J. Phys. Chem. B **117**, 11397 (2013).

[15] L. Bocquet and J.-L. Barrat, Hydrodynamic Boundary Conditions and Correlation Functions of Confined Fluids, Phys. Rev. Lett. **70**, 2726 (1993).

[16] L. Bocquet and E. Charlaix, Nanofluidics, from bulk to interfaces, Chem. Soc. Rev. **39**, 1073 (2010).

[17] A. Delville, Structure of liquids at a solid interface: An application to the swelling of clay by water, Langmuir **8**, 1796 (1992).

[18] P. Simonnin, V. Marry, B. Noetinger, C. Nieto-Draghi, and B. Rotenberg, Mineral- and ion-specific effects at clay-water interfaces: Structure, diffusion, and hydrodynamics, J. Phys. Chem. C **122**, 18484 (2018).

[19] A. Russo, M. A. Duran-Olivencia, S. Kalliadasis, and R. Hartkamp, Macroscopic relations for microscopic properties at the interface between solid substrates and dense fluids, J. Chem. Phys. **150**, 214705 (2019).

[20] S. Granick, Motions and relaxations of confined liquids, Science **253**, 1374 (1991).

[21] Y. Zhu and S. Granick, Viscosity of Interfacial Water, Phys. Rev. Lett. **87**, 096104 (2001).

[22] A. Dhinojwala and S. Granick, Relaxation time of confined aqueous films under shear, J. Am. Chem. Soc. **119**, 241 (1997).

[23] H.-W. Hu, G. A. Carson, and S. Granick, Relaxation Time of Confined Liquids under Shear, Phys. Rev. Lett. **66**, 2758 (1991).

[24] P. Liu, E. Harder, and B. J. Berne, On the calculation of diffusion coefficients in confined fluids and interfaces with an application to the liquid-vapor interface of water, J. Phys. Chem. **108**, 6595 (2004).

[25] V. Marry, B. Rotenberg, and P. Turq, Structure and dynamics of water at a clay surface from molecular dynamics simulation, Phys. Chem. Chem. Phys. **10**, 4802 (2008).

[26] M. S. Green, Markoff random processes and the statistical mechanics of time-dependent phenomena, J. Chem. Phys. **20**, 1281 (1952).

[27] M. S. Green, Markoff random processes and the statistical mechanics of time-dependent phenomena. II. irreversible processes in fluids, J. Chem. Phys. **22**, 398 (1954).

[28] R. Kubo, Statistical-mechanical theory of irreversible processes. I. general theory and simple applications to magnetic and conduction problems, J. Phys. Soc. Jpn. **12**, 570 (1957).

[29] R. Zwanzig, Time-correlation functions and transport coefficients in statistical mechanics, Annu. Rev. Phys. Chem. **16**, 67 (1965).

[30] C. Y. Gao and D. T. Limmer, Transport coefficients from large deviation functions, Entropy **19**, 571 (2017).

[31] C. Y. Gao and D. T. Limmer, Nonlinear transport coefficients from large deviation functions, J. Chem. Phys. **151**, 014101 (2019).

[32] P. Español and I. Zúñiga, On the definition of hydrodynamic variables, J. Chem. Phys. **131**, 164106 (2009).

[33] P. Español, J. Anero, and I. Zúñiga, Microscopic derivation of discrete hydrodynamics, J. Chem. Phys. **131**, 244117 (2009).

[34] P. Español and A. Donev, Coupling a nano-particle with isothermal fluctuating hydrodynamics: Coarse-graining from microscopic to mesoscopic dynamics, J. Chem. Phys. **143**, 234104 (2015).

[35] E. M. Lifshitz and L. P. Pitaevskii, *Statistical Physics Part 2* (Butterworth-Heinemann, Oxford, 2006).

[36] A. Donev, A. J. Nonaka, C. Kim, A. L. Garcia, and J. B. Bell, Fluctuating hydrodynamics of electrolytes at electroneutral scales, Phys. Rev. Fluids **4**, 043701 (2019).

[37] J.-P. Péraud, A. Nonaka, J. B. Bell, A. Donev, and A. L. Garcia, Fluctuation-enhanced electric conductivity in electrolyte solutions, Proc. Natl. Acad. Sci. U. S. A. **114**, 10829 (2017).

[38] B. Palmer, Coarse-grained hydrodynamics from correlation functions, Phys. Rev. E **97**, 022106 (2018).

[39] J.-P. Boon and S. Yip, *Molecular Hydrodynamics* (Dover, New York, 1980).

[40] D. Forster, *Hydrodynamic Fluctuations, Broken Symmetry, and Correlation Functions* (Benjamin/Cummings, Reading, MA, 1975).

[41] C. Gardiner, *Handbook of Stochastic Methods for Physics, Chemistry and the Natural Sciences*, (Springer, New York, 1985).

[42] C. Hoheisel and R. Vogelsang, Thermal transport coefficents for one- and two-component liquids for time correlation functions computed by molecular dynamics, Comput. Phys. Rep. **8**, 1 (1988).

[43] B. Hess, Determining the shear viscosity of model liquids from molecular dynamics simulations, J. Chem. Phys. **116**, 209 (2002).

[44] B. Palmer, Transverse-current autocorrelation-function calculations of the shear viscosity for molecular liquids, Phys. Rev. E **49**, 359 (1994).

[45] B. Palmer, Calculation of thermal-diffusion coefficients from plane-wave fluctuations in the heat-energy density, Phys. Rev. E **49**, 2049 (1994).

[46] T. Munson, J. Sarich, S. Wild, S. Benson, and L. C. McInnes, Toolkit for advanced optimization (tao) users manual, Technical Report No. ANL/MCS-TM-322-Revision 3.5, Argonne National Laboratory, 2014 (unpublished).

[47] S. Balay, S. Abhyankar, M. F. Adams, J. Brown, P. Brune, K. Buschelman, L. Dalcin, V. Eijkhout, W. D. Gropp, D.

Kaushik, M. G. Knepley, D. A. May, L. C. McInnes, R. T. Mills, T. Munson, K. Rupp, P. Sanan, B. F. Smith, S. Zampini, and H. Zhang, PETSc users manual, Technical Report No. ANL-95/11-Revision 3.9, Argonne National Laboratory, 2018 (unpublished).

[48] S. Balay, W. D. Gropp, L. C. McInnes, and B. F. Smith, Efficient management of parallelism in object oriented numerical software libraries, in *Modern Software Tools in Scientific Computing*, edited by E. Arge, A. M. Bruaset, and H. P. Langtangen (Birkhäuser, Boston, 1997), pp. 163–202.

[49] I. R. McDonald and K. Singer, Calculation of thermodynamic properties of liquid argon from lennard-jones parameters by a monte carlo method, Discuss. Faraday Soc. **43**, 40 (1967).

[50] M. P. Allen and D. J. Tildesley, *Computer Simulation of Liquids* (Clarendon, Oxford, 1987).

[51] G. Berghold, C. J. Mundy, A. H. Romero, J. Hutter, and M. Parrinello, General and efficient algorithms for obtaining maximally localized wannier functions, Phys. Rev. B **61**, 10040 (2000).

[52] M. Abramowitz and I. Stegun, *Handbook of Mathematical Functions* (Dover, New York, 1972).

[53] Wolfram Research, Inc, Mathematica, Version 12.1, Champaign, IL (2020), https://www.wolfram.com/mathematica.